Segregation Stabilizes Nanocrystalline Bulk Steel with Near Theoretical Strength

Yujiao Li,[1,2,*] Dierk Raabe,[1,†] Michael Herbig,[1] Pyuck-Pa Choi,[1] Shoji Goto,[1,3] Aleksander Kostka,[1] Hiroshi Yarita,[4] Christine Borchers,[2] and Reiner Kirchheim[1,2]

[1]*Max-Planck Institut für Eisenforschung, Max-Planck-Strasse 1, D-40237 Düsseldorf, Germany*

[2]*Georg-August-Universität Göttingen, Friedrich-Hund-Platz 1, D-37077 Göttingen, Germany*

[3]*Akita University, Tegata Gakuencho, Akita 010-8502, Japan*

[4]*Suzuki Metal Industry Co. LTD., Narashino, Chiba 275-8577, Japan*

(Received 8 February 2014; revised manuscript received 3 July 2014; published 5 September 2014)

Grain refinement through severe plastic deformation enables synthesis of ultrahigh-strength nanostructured materials. Two challenges exist in that context: First, deformation-driven grain refinement is limited by dynamic dislocation recovery and crystal coarsening due to capillary driving forces; second, grain boundary sliding and hence softening occur when the grain size approaches several nanometers. Here, both challenges have been overcome by severe drawing of a pearlitic steel wire (pearlite: lamellar structure of alternating iron and iron carbide layers). First, at large strains the carbide phase dissolves via mechanical alloying, rendering the initially two-phase pearlite structure into a carbon-supersaturated iron phase. This carbon-rich iron phase evolves into a columnar nanoscaled subgrain structure which topologically prevents grain boundary sliding. Second, Gibbs segregation of the supersaturated carbon to the iron subgrain boundaries reduces their interface energy, hence reducing the driving force for dynamic recovery and crystal coarsening. Thus, a stable cross-sectional subgrain size < 10 nm is achieved. These two effects lead to a stable columnar nanosized grain structure that impedes dislocation motion and enables an extreme tensile strength of 7 GPa, making this alloy the strongest ductile bulk material known.

DOI: 10.1103/PhysRevLett.113.106104 PACS numbers: 81.07.Bc, 81.40.Lm

Following the principle of "smaller is stronger" [1,2] grain refinement is a strategy for improving the strength of metals. Severe plastic deformation (SPD) is an efficient technique for producing ultrahigh-strength nanostructured materials [3–6]. SPD induces a large density of dislocations into the material, leading to a network of low-angle grain boundaries at lower strains and turning some of them into high-angle grain boundaries at higher strains so that the grain size is refined [7]. However, deformation-driven grain refinement into the nm regime is typically prevented by dynamic recovery, which is characterized by dislocation annihilation and capillary-driven (sub-) grain coarsening. Competition between grain refinement and coarsening leads to grain size saturation at several hundred nm in pure metals [8]. The deformed materials typically reach only 1/10 to 1/3 of the theoretical strength [9–11]. Hence, the key challenge in producing mechanically strong nanostructured materials via severe plastic deformation lies in the suppression of dynamic recovery so that the grain size can be further refined and rendered stable.

Mechanical alloying [12] offers potential for further progress in that context: For example, ball milling of iron and graphite results in 3D equiaxed ferrite grains with 10 nm size [13–15]. Segregation of carbon to grain boundaries decreases the grain boundary energy via the Gibbs adsorption theorem, reducing the driving force for grain coarsening [16,17]. A similar grain structure was achieved in a pearlitic wire subjected to high pressure torsion (HPT) [18]. However, when the grain size is reduced to several nanometers, another challenge arises, namely, that the principle of smaller is stronger breaks down [19]. Below a certain grain size further grain refinement reduces the strength of materials, because grain boundary related softening such as grain boundary sliding and grain rotation may occur in materials with 3D equiaxed nanograins [19]. For instance, both materials mentioned above [13,14,18] exhibit an equivalent maximum tensile strength of 4 GPa, which is about 3 GPa below the strength of the material studied here.

Here we report about a case where carbon segregation to 2D columnar nanoscaled subgrain boundaries in ferrite (iron phase with body centered cubic structure) has enabled us to overcome both challenges, namely, grain coarsening and interface sliding. The columnar structure has been produced by severe cold drawing of a pearlitic steel wire. Undeformed pearlite consists of alternating layers of ferrite and cementite, here used with hypereutectoid composition (Fe-0.98 C-0.31Mn-0.20Si-0.20Cr-0.01Cu-0.006 P-0.007 S, wt.%). Cementite is an iron carbide with Fe_3C stoichiometry and orthorhombic crystal structure. The hypereutectoid concentration lies slightly above the eutectoid temperature-composition intersection where the austenite phase transforms directly into a layered ferrite-cementite solid. This is referred to as a pearlitic reaction. The wires were austenitized at 1223 K for 80 s followed by a pearlitic transformation at 853 K for 20 s. The controlled

transformation in the high temperature pearlite regime is referred to as patenting. Austenite is a high temperature solid solution iron-carbon phase with face centered cubic structure. Starting from a diameter of 0.54 mm and interlamellar spacing of 67 nm the pearlitic wires were then cold drawn to true (logarithmic) strains of 0 (as-patented), 1.06, 1.96, 3.10, 4.19, 5.10, 6.23, and 6.52, respectively.

The highest total wire drawing strain (6.52) leads to a tensile strength of 7 GPa, which is stronger than any other bulk (volume) material available today. Tensile tests were performed at room temperature and constant strain rate 2×10^{-3} s^{-1}. The true tensile strain is determined by $\epsilon = \ln(l_0 + \Delta l/l_0)$, where l_0 and Δl are the initial gauge length and the length change of the wires, respectively. Length changes due to the initial adjustment between wires and deformation machine was subtracted from the total measured Δl. The true tensile stress is determined by $\sigma = (F/S_0)\exp(\epsilon)$, where F is the force and S_0 the initial cross section of the wires. The measurement error for σ is within $\pm 8\%$ due to fluctuation of S_0.

Figure 1(a) shows the true tensile stress-strain curves of the wires predeformed to various strains ϵ_d between 1.06 and 6.52. The initial wire ($\epsilon_d = 0$) shows a maximum tensile strength above 1 GPa. With higher ϵ_d the maximum tensile strength significantly increases. One has to note that the nearly linear regime indicated by the red dotted triangle does not show the elastic regime but marks the plastic slope, i.e., the strain hardening. The elastic slope (elastic modulus) is much higher as indicated by the green triangle. The elastic regime cannot be resolved from this diagram with sufficient accuracy though. The fracture surface [SEM image in Fig 1(a)] shows equiaxed dimples. This is a typical feature of plastic deformation under uniaxial tensile loading. Figure 1(b) shows the dependence of the maximum tensile strength σ [black solid circles, taken from Fig. 1(a)], work hardening rate $d\sigma/d\epsilon$ (red dashed line) and area reduction (blue open circles) on the total true drawing strain. Note that the abscissa shows the total strain, i.e., the tensile strain plus the preceding wire drawing strain. At $\epsilon_d < 4$ the work hardening rate increases strongly with ϵ_d. In this regime the reduction in cross section area lies between 0.4–0.6. For $\epsilon_d > 4$ a diminishing strain hardening together with an abrupt loss in tensile reduction of area (below 0.2) occurs, suggesting a significant microstructural change, as will be addressed later. Figure 1(c) compares the maximum tensile strength of nearly 7 GPa at $\epsilon_d = 6.52$ (red solid squares) with literature data for iron whiskers and other ultrahigh-strength materials. The comparison reveals that the material exhibits the highest experimentally

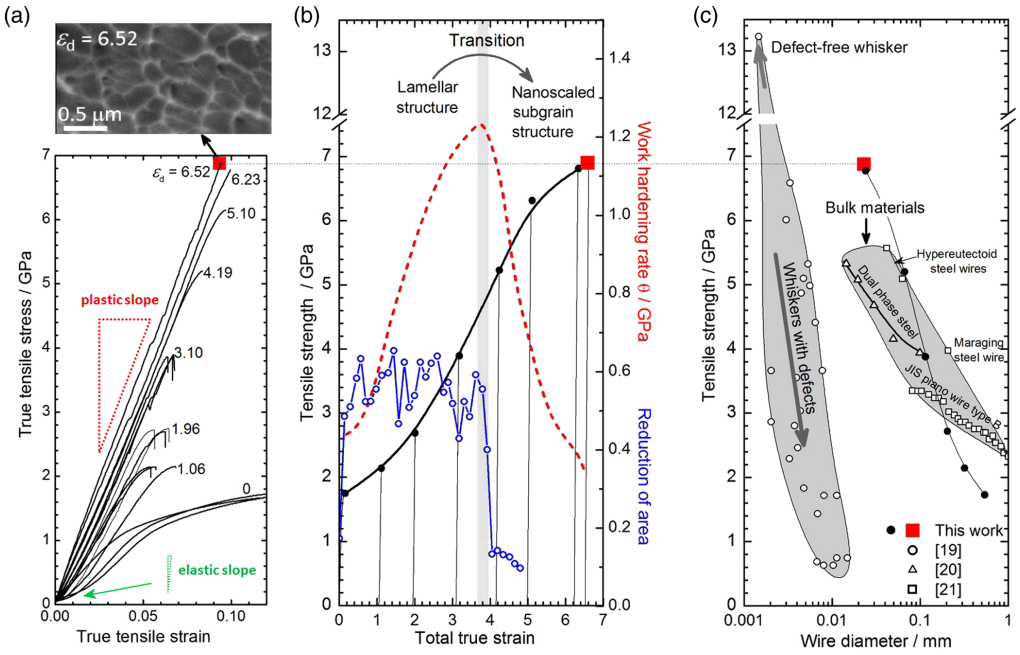

FIG. 1 (color online). Strength and ductility of cold-drawn pearlite. (a) True tensile stress-strain curves of cold-drawn wires for various drawing strains. The preceding true wire strain is indicated for each stress-strain curve. Note that the near-linear regime indicated by the red dotted triangle is not the elastic, but the plastic slope (strain hardening). The elastic slope (elastic modulus) is much higher as indicated by the green triangle. It cannot be resolved from this diagram. The inset shows a SEM image of a fracture surface after the tensile test of the most extremely cold-drawn wire, revealing dimples that indicate plastic deformation prior to fracture. (b) Variations of tensile strength σ (thick dark line), work hardening rate $d\sigma/d\epsilon$ (dashed red line), and reduction of area (blue circles) during cold drawing of as-patented wires showing the transition from ductile to less-ductile behavior. Note that the abscissa shows the total true strain, i.e., the tensile strain plus the preceding wire drawing strain. (c) Comparison of tensile strength versus wire diameter for various high strength materials [20–22], showing that the current cold-drawn ($\epsilon_d = 6.52$) pearlitic wire is the strongest bulk material known to date.

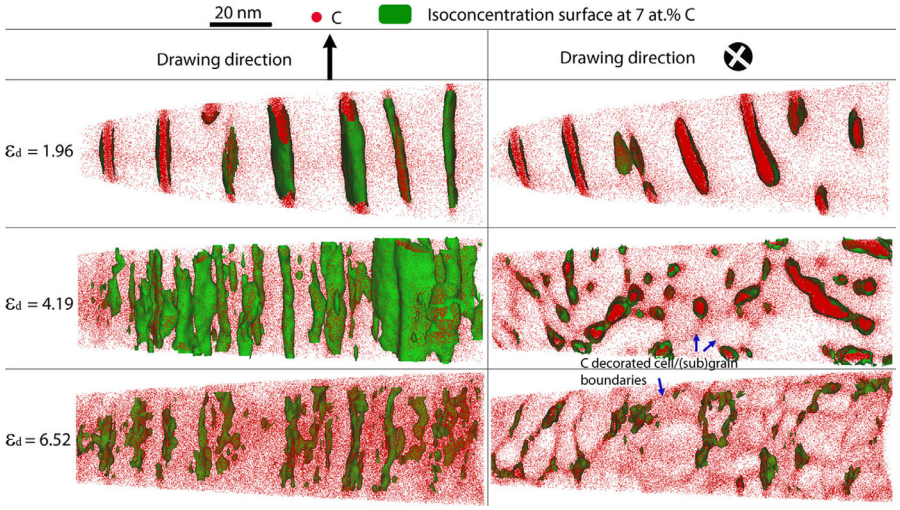

FIG. 2 (color online). Atom probe tomographic characterization of pearlitic steel wires cold drawn to different drawing strains. 3D carbon atom maps in both longitudinal (parallel to the drawing direction) and transverse cross section views (perpendicular to the drawing direction). Blue arrows mark some of the subgrain boundaries decorated with carbon atoms.

measured tensile strength among all known ductile bulk materials.

Characterization of the samples was conducted using a local electrode atom probe (LEAP 3000X HR™, Cameca). Samples for atom probe tomography analyses were prepared using a dual beam focused-ion-beam (FIB) (FEI Helios) [23,24]. Figure 2 shows 3D carbon atom maps in longitudinal (left) and cross-sectional (right) views of samples drawn to low, medium, and extremely high strains. Carbon-enriched regions identified by green isoconcentration surfaces represent cementite, with the carbon-depleted regions being ferrite. With increasing drawing strain, first, the volume fraction of cementite continuously decreases due to its mechanically driven chemical decomposition [15,17,23], and second, the carbon atoms are released from the dissolving cementite and are mechanically alloyed into the ferrite. This leads to a deformation-driven carbon supersaturation of the ferrite. Third, the initially two-phase lamellar pearlite structure evolves, due to its dissolving cementite layers, into a carbon-decorated ferrite subgrain structure, as is visualized by the carbon segregation at the ferrite boundaries (marked by blue arrows). At $\epsilon_d = 4.19$ a transition from the lamellar structure to the dislocation subgrain structure is observed. At $\epsilon_d = 6.52$ the subgrains exhibit a nearly equiaxed shape with sizes d_{Sub} below 10 nm in the transverse cross section of the wire. Finally, the subgrains assume a columnar morphology along the drawing direction (see also animations in the Supplemental Material [25]).

To test the stability of the nanosized subgrain structure, samples cold drawn to $\epsilon_d = 6.52$ were annealed for 30 min at 150 and 250 °C, respectively. The bright field TEM images shown in Figs. 3(a) and 3(b) prove that the typical curled nanoscaled morphology observed in transverse cross sections, typically developed during cold drawing of body centered cubic metals, prevails in both heat treated samples. The distributions of the low- and high-angle grain boundaries as well as phase identification are analyzed by scanning nanobeam TEM diffraction using automated crystal orientation and phase mapping [26] [Figs. 3(c) and 3(d)]. The subgrains exhibit in this cross-sectional view nearly equiaxed shape and a subgrain size of 11 ± 1.38 nm for both annealed samples; i.e., subgrain coarsening is marginal. The line fraction of low-angle grain boundaries (green lines with misorientations 3°–15°) is about 40%. These results confirm the atom probe tomography observations of a stable deformation-induced nanoscaled subgrain structure. The orientation identification performed by

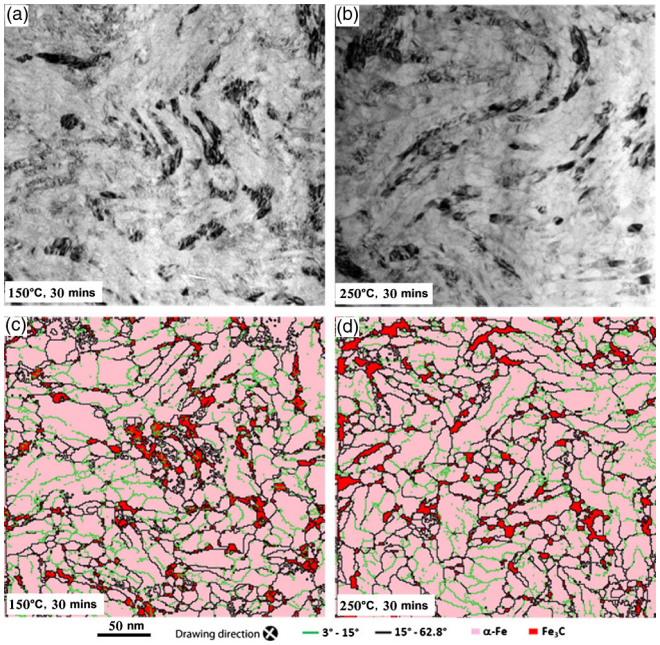

FIG. 3 (color online). Analysis of the cold-drawn pearlitic wire ($\epsilon_d = 6.52$) followed by annealing for 30 min at 150 and 250 °C, respectively, in transverse cross section (view into drawing direction). (a) and (c) Correlative bright field TEM image and phase maps obtained via scanning nanobeam TEM diffraction for 150 °C, respectively. (b) and (d) Analogue to (a) and (c) for 250 °C.

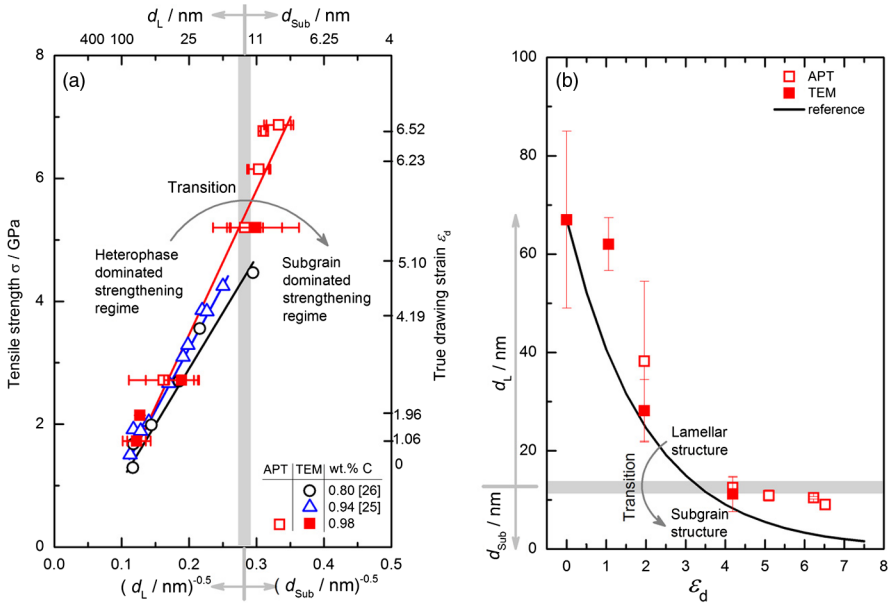

FIG. 4 (color online). Tensile strength versus the reciprocal square roots of lamellar spacing d_L and subgrain size d_{Sub} as well as their evolution with drawing strain measured by TEM and atom probe tomography. Literature data for eutectoid (0.80 wt. % C) [28] and hypereutectoid (0.94 wt. % C) pearlitic steel [27] are shown for comparison. (a) Tensile strength versus the reciprocal square root of d_L and, respectively, d_{Sub}. (b) Evolution of d_L and d_{Sub} with drawing strain; the dark reference line sets the theoretical minimum subgrain sizes $d_{\mathrm{L,min}}$ calculated by $\epsilon_d = \ln(d_{L0}^2/d_{\mathrm{L,min}}^2)$.

the nanobeam TEM diffraction method shows that no overlap of subgrains occurs in the direction normal to the TEM observation direction, confirming the atom probe tomography results of a columnar structure.

Figure 4(a) shows the measured tensile strengths versus the square roots of d_L and d_{Sub} plotted together with data taken from [27,28] for comparison (Hall-Petch relation). In the present context the Hall-Petch relationship has been widely used to describe the strength increase of pearlite by reducing the average lamellar spacing between the ferrite and the cementite phases. More specifically, the strength increase was observed to be inversely proportional to the square root of the average lamellar spacing. This observation was attributed to the fact that internal interfaces impede dislocation movement and hence obstruct plastic deformation. This leads to an increase in strength. The literature data measured on samples with lower carbon content than the alloys probed here, cold drawn to relatively low strains, indeed follow such a Hall-Petch relation; i.e., the lamellar structure seems to be dominant for the material's strength.

Surprisingly, the same Hall-Petch relation also holds for our current data in the regime $\epsilon_d > 4.19$, where the cementite has been essentially dissolved so that the nano-scaled subgrain structure and not the lamellar structure prevails. In addition, the Hall-Petch slope is the same as that in the lamellar structure dominated regime $\epsilon_d < 4.19$. This result indicates that, first, the ultrahigh strength of 7 GPa is not due to a lamellar structure but to the carbon-supersaturated ferrite subgrain structure. Second, the C-decorated boundaries (both low-angle and high-angle grain boundaries) have a comparable strengthening effect as the phase boundaries between ferrite and cementite.

For comparison, severe cold drawing of a pure iron wire to a true strain of 7 yields a subgrain size of only 100 nm and a tensile strength of 1.2 GPa [29]. In contrast, cold drawing of the current pearlite wire to a strain of 6.52 results in a subgrain size < 10 nm in combination with an enormous strength of 7 GPa. Why can the subgrain size in pearlite, when mechanically alloyed into carbon-supersaturated ferrite by heavy cold drawing, be refined to a value 1 order of magnitude below that in pure iron? The grain size in pure metals resulting from severe plastic deformation is determined by the competition of grain refinement and capillary driven coarsening. In pearlite, the initial interlamellar spacing between ferrite and cementite is about 67 nm, which is already smaller than the minimum subgrain size that could be formed in pure metals. Thus, dislocation motion and storage is no longer determined by dislocation self-organization but confined by the ferrite-cementite interfaces. The strongly reduced mean free path of dislocations leads to enhanced rates of dislocation multiplication and work hardening inside the ferrite [Fig. 1(b)]. As a result, the formation rate of dislocation boundaries at the ferrite-cementite interface increases, because dislocations get stored there. At larger strains the mechanically driven decomposition of cementite would at first be expected to reduce the strength of the material, as the confinement of dislocation motion by cementite is no longer given so that dynamic recovery would promote subgrain coarsening. However, such coarsening cannot happen in the present case because the dissolving cementite releases carbon that decorates and stabilizes the supersaturated ferrite grain boundaries [16].

The effect of this intense carbon decoration on reducing dynamic recovery of the nano-scaled subgrain structure can be estimated as follows: When assuming that cementite would not decompose and no dynamic recovery of subgrains would occur, the cross-sectional subgrain size would

equal the lamellar spacing. The latter scales with the drawing strain, hence, following $\epsilon_d = \ln(d_{L0}^2/d_{\mathrm{L,min}}^2)$ owing to deformation compatibility [27], where d_{L0} is the initial lamellar spacing and $d_{\mathrm{L,min}}$ sets the theoretical minimum subgrain size at a given drawing strain ϵ_d. Figure 4(b) compares the measured subgrain sizes with the theoretical minimum values ($d_{\mathrm{L,min}}$, black line). In the regime $\epsilon_d < 4.19$ where the initially lamellar pearlitic structure still prevails, the measured lamellar spacings d_L agree well with the calculated values. In the subgrain dominated regime $\epsilon_d > 4.19$ the measured subgrain sizes lie above the theoretical values and show a tendency of size saturation. This indicates the occurrence of slight dynamic recovery. It also explains the drop in work hardening rate [Fig. 1(b)] observed at $\epsilon_d = 4.19$. However, despite the slight difference between the measured subgrain sizes (9 nm) and the theoretical limit (3 nm), it is evident that dynamic recovery has been reduced by carbon segregation due to the Gibbs adsorption effect which reduces the interface energy and due to carbon-drag preventing dislocation relaxation. Besides the grain-size strengthening the atom probe tomography maps reveal (Fig. 2, Supplemental Material [25]) that the grains cannot undergo grain boundary sliding owing to their 2D (columnar) morphology.

In revisiting the microstructural evolution of pearlite during drawing it is found that the second phase cementite plays an essential role. At lower drawing strains cementite facilitates fast reduction of the subgrain size by hindering dislocation motion through the fine lamellar spacing. At larger strains cementite chemically decomposes via mechanical alloying and acts as a supplier of carbon, which segregates to the ferrite subgrain boundaries stabilizing the nanoscaled ferrite structure. The Hall-Petch relation between the substructure and the observed strength increase holds for our current data in the strain regime $\epsilon_d > 4.19$ where cementite has been essentially dissolved. This means that the carbon-supersaturated and stabilized nanoscaled ferrite subgrain structure and not the lamellar structure is responsible for the ultrahigh strength of 7 GPa. These findings reveal an essential type of strengthening and may stimulate new ideas for the design of ultrahigh strength materials.

We are grateful to the Deutsche Forschungsgemeinschaft for funding (SFB 602, KI230/34-1, SFB 761). Support by the Alexander von Humboldt Stiftung is acknowledged by S. G.

*Corresponding author.
y.li@mpie.de
†Corresponding author.
d.raabe@mpie.de

[1] K. S. Kumar, H. Van Swygenhoven, and S. Suresh, Acta Mater. **51**, 5743 (2003).
[2] J. R. Weertman, MRS Bull. **29**, 616 (2004).
[3] R. Z. Valiev and T. G. Langdon, Prog. Mater. Sci. **51**, 881 (2006).
[4] A. P. Zhilyaev and T. G. Langdon, Prog. Mater. Sci. **53**, 893 (2008).
[5] Y. Saito, H. Utsunomiya, N. Tsuji, and T. P. Sakai, Acta Mater. **47**, 579 (1999).
[6] K. Lu and N. Hansen, Scr. Mater. **60**, 1033 (2009).
[7] R. Z. Valiev, R. K. Islamgaliev, and I. V. Alexandrov, Prog. Mater. Sci. **45**, 103 (2000).
[8] R. Pippan, S. Scheriau, A. Taylor, M. Hafok, A. Hohenwarter, and A. Bachmaier, Annu. Rev. Mater. Res. **40**, 319 (2010).
[9] B. Wu, A. Heidelberg, and J. Boland, Nat. Mater. **4**, 525 (2005).
[10] G. Richter, K. Hillerich, D. S. Gianola, R. Monig, O. Kraft, and C. A. Volkert, Nano Lett. **9**, 3048 (2009).
[11] S. S. Brenner, Acta Metall. **4**, 62 (1956).
[12] D. Raabe, P. Cho, Y. J. Li, A. Kostka, X. Sauvage, F. Lecouturier, K. Hono, R. Kirchheim, R. Pippan, and D. Embury, MRS Bull. **35**, 982 (2010).
[13] A. Xu, M. Umemoto, and K. Tsuchiya, Mater. Trans., JIM **43**, 2205 (2002).
[14] S. Takaki, T. Tsuchiyama, K. Nakashima, H. Hidaka, K. Kawasaki, and Y. Futamura, Met. Mater. Int. **10**, 533 (2004).
[15] Y. Z. Chen, A. Herz, Y. J. Li, C. Borchers, P. Choi, D. Raabe, and R. Kirchheim, Acta Mater. **61**, 3172 (2013).
[16] R. Kirchheim, Acta Mater. **55**, 5129 (2007).
[17] M. Herbig, D. Raabe, Y. J. Li, P. Choi, and S. Zaefferer, and S. Goto, Phys. Rev. Lett. **112**, 126103 (2014).
[18] Y. Ivanisenko, W. Lojkowski, R. V. Valiev, and H. J. Fecht, Acta Mater. **51**, 5555 (2003).
[19] J. Schiϕtz, D. D. Di Tolla, and K. W. Jacobsen, Nature (London) **391**, 561 (1998).
[20] S. S. Brenner, J. Appl. Phys. **27**, 1484 (1956).
[21] H. K. D. H. Bhadeshia and H. Harada, Appl. Surf. Sci. **67**, 328 (1993).
[22] H. Tashiro, Nippon Steel Technical Report **80**, 6 (1999).
[23] Y. J. Li, P. Choi, S. Goto, C. Borchers, S. Westerkamp, D. Raabe, and R. Kirchheim, Acta Mater. **59**, 3965 (2011).
[24] Y. J. Li, P. Choi, S. Goto, C. Borchers, D. Raabe, and R. Kirchheim, Acta Mater. **60**, 4005 (2012).
[25] See Supplemental Material at http://link.aps.org/supplemental/10.1103/PhysRevLett.113.106104 for Video 1: 3D Atom Probe Tomography reconstruction along the z-axis which is perpendicular to the drawing direction for the cold-drawn wire at $\epsilon_d = 1.96$. Green-colored iso-concentration surfaces for C at 7 at. % are plotted. C atoms are represented by red dots. Video 2: Analogous to Video 1 but for $\epsilon_d = 4.19$. Video 3: Analogous to Video 1 but for $\epsilon_d = 6.52$.
[26] P. Moeck, S. Rouvimov, E. F. Rauch, M. Veron, H. Kirmse, I. Häusler, W. Neumann, D. Bultreys, Y. Maniette, and S. Nicolopoulos, Cryst. Res. Technol. **46**, 589 (2011).
[27] J. D. Embury and R. M. Fisher, Acta Metall. **14**, 147 (1966).
[28] Y. Z. Chen, G. Csiszár, J. Cizek, S. Westerkamp, C. Borchers, T. Ungr, S. Goto, F. Liu, and R. Kirchheim, Metall. Mater. Trans. A **44**, 3882 (2013).
[29] G. Langford and M. Cohen, J. Energy Resour. Technol. **62**, 623 (1969).